대한기계학회 2000년도 추계학술대회논문집 B pp. 544~549 KSME 00F204

The Effects of Nonequilibrium Condensation on Shock/Boundary Layer Interaction

H.D.Kim*, K.H.Lee**, and T.Setoguchi***

비평형응축이 충격파와 경계층의 간섭에 미치는 영향

김희동*, 이권희**, T.Setoguchi***

Key Words : Keywords: Compressible Flow, Nonequilibrium Condensation, Shock Wave, Transonic Flow, Shock Oscillation

Abstract

The effects of nonequilibrium condensation on the shock boundary layer interaction over a transonic bump model were investigated experimentally and numerically. An experiment was conducted using a supersonic indraft wind tunnel. A droplet growth equation was incorporated into two-dimensional Navier-Stokes equation systems. Computations were carried out using a third-order MUSCL type TVD finite-difference scheme with a second-order fractional time step. Computations compared with the experimental results. Nonequilibirum condensation suppressed the boundary layer separation and the pressure fluctuations due to the shock boundary layer interaction. Especially the nonequilibrium condensation was helpful to suppress the high frequency components of the pressure fluctuations.

1. Introduction

A rapid expansion of moist air or steam is presented in the flows through a transonic or supersonic nozzle and a turbine cascade and often gives rise to non-equilibrium condensation. The whole flow field is strongly affected by the latent heat released by the condensation of water vapor. The condensation phenomenon is essentially an irreversible process leading to appreciable entropy rise. If the heat release exceeds a certain critical value, it is known that the nonequilibrium condensation leads to a discontinuous change of thermodynamic flow properties.[1-4] Condensation shock wave has long been of scientific and academic research topic, and many thermodynamic and fluid dynamic aspects of the nonequilibrium condensation and condensation shock wave are well known now. The condensation shock wave almost always leads to large energy losses as well as flow instability due to the condensation shock wave oscillations, thereby affecting the whole performance of system.[5-6]

Many experimental and numerical investigations have been made to understand the relationship between shock wave and nonequilibrium condensation.[5-8] Much has been known about the effects of *nonequilibrium condensation and condensation shock* wave on flow field. With the nonequilibrium condensation upstream of the shock wave, the flow Mach number reduces due to total pressure loss and latent heat released by the nonequilibrium condensation, consequently leading to suppression of shock-induced boundary layer separation. In addition, the fine droplets generated by the nonequilibrium condensation can alleviate the flow fluctuations downstream of the shock wave. The nonequilibrium condensation leads to total pressure losses, which influence the interaction between shock wave and boundary layer. However the detailed effects of nonequilibrium condensation on the shock boundary layer interaction have not been fully understood yet. Moreover there are still many unknown problems for the effects of the nonequilibrium condensation on the flow fluctuations occurring behind the shock wave. The major objectives of the current study are to investigate the effects of the nonequilibrium condensation on the shock wave boundary layer interaction which occurs in a transonic flow over a bump model. A nonequilibrium condensing flow was made by an expansion of moist air over several bump models. An experiment was carried out to explore the effects of the initial conditions of the moist air flow and the bump configurations on the shock wave and flow fluctuations. Computations were made to predict the experimental results. Naveir-Stokes equations were solved numerically using a 3rd order MUSCL type TVD finite difference

* professor, Andong National University.
** BK21 researcher, Andong National University.
*** professor, Saga University, Japan

scheme with a 2nd order fractional step for time integration.

2. Experimental Facility and Procedure

A supersonic indraft wind tunnel is used to generate nonequilibirum condensation of atmospheric moist air in test section. A vacuum chamber with a volume of $6m^3$ is connected to the test section, through which the controlled moist air in the upstream plenum chamber flows into the vacuum chamber. As schematically shown in Fig.1, two bump models with a radius of 40mm and 200mm are installed on the lower wall of the test section. The chord length l of two bump models is 34.9mm and 76.9mm, respectively, but the height of the two models is fixed at 4.0mm. A multiple of pressure transducers are mounted flush on the bump models.

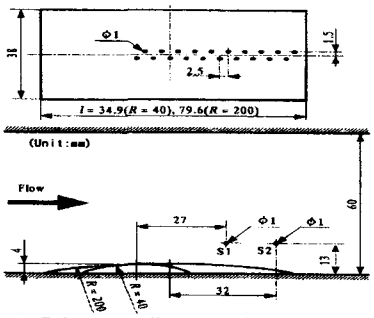

Fig. 1 Schematic diagram of bump model

Time-mean and time dependent pressures are measured using the pressure transducers. In addition, a schlieren optical system is used to observe the flow field over the bump models. In order to investigate the surface flow mechanism over the bump models, a shear sensitive liquid crystal (Merck Industrial Chemicals, TI622) is used for flow visualization. A dryer system and heater system controls the initial stagnation conditions of the atmospheric air charged into the upstream plenum chamber. The stagnation temperature and relative humidity are measured by using a thermometer and a humidity indicator. The steady flow over the bump models lasting for about 5 seconds is enough to implement the measurements required in the present work. The stagnation pressure P_{01} in the upstream plenum chamber is kept constant by 102kPa, and the stagnation temperature T_{01} is set at 298K in the present experiment. The initial degree of supersaturation S_{01}, as is usually defined as the ratio vapour pressure to the equilibrium saturation pressure corresponding to the plenum chamber temperature is varied in the range from 0.24 to 0.80 where is enable to occur nonequilibrium condensations in the transonic flows over bump models. The static pressure P in the upstream of the bump model is measured. P/P_{01} (=0.719) gives the flow Mach number of 0.735.

3. Navier-Stokes Computation

Very like general two-phase flow analysis, several of assumptions are made for the present computations. There is no velocity slip and no temperature difference between condensate particles and medium gas flows, and due to very small condensate particles the effect of the particles on pressure field can be neglected within the accuracy of the present computations. The governing equations are unsteady two-dimensional, compressible, Navier-Stokes equations and a droplet growth equation[9] written in the Cartesian coordinate system (x,y). The governing equations are non-dimensionalized using the reference values at the upstream plenum conditions and are in details given in Ref[10,11]. Values of accommodation coefficient[12] for nucleation, condensation coefficient[13] and surface tension coefficient[14] are 106, 0.9 and 1.29, respectively. Baldwin-Lomax model is used as a turbulence closure model in the present computations. The governing equation systems are mapped from the physical plane of reference frame (x,y) into a computational plane of reference $(\xi\ \eta)$ using a general transformations. A third order High resolution MUSCL type TVD finite difference scheme with a second order fractional step for time integration is applied to solve the governing equation systems and the droplet growth equation. A second order centered difference scheme is used for viscous terms. The detailed computational procedure is referred to Ref[10,11] Fig.2 shows computational grid system. The grids contain 200 divisions in ξ-direction and 60 divisions in η-direction. The minimum dimensional length is 0.0717mm closest to solid wall boundaries. Free boundary conditions are applied to both the inlet and exit boundaries. Adiabatic no-slip velocity is applied to the solid wall boundaries, in which condensate mass fraction g is assumed at g=0 on the walls. The conservative vector variables at the fictitious cells at both the inlet and exit boundaries are constrained with Riemann invariant. The value of CFL number is fixed at 0.98 through whole computations.

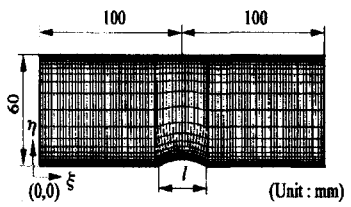

Fig. 2 Computational grid

4. Results and Discussion

4.1 Flow visualization

Fig.3 shows schlieren pictures for the transonic flows over R=40 and 200mm bump models.

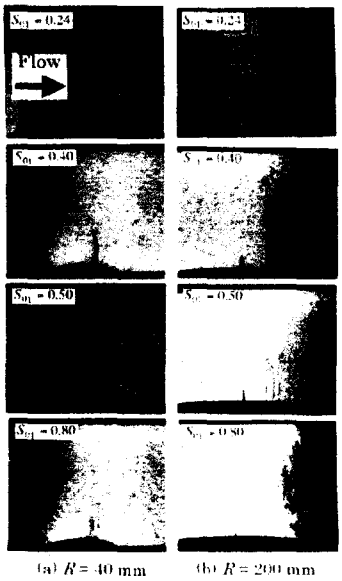

Fig. 3 Schlieren pictures

The initial degree of supersaturation S_{01} was varied from 0.24 to 0.80. Note that for S_{01}=0.24 the flow is assumed to be a dry air in the present study. A weak normal transonic shock wave is clearly visible over the bump model. It is found that influences the shock structure is influenced by the bump model configuration significantly. For two bump models it seems that the shock wave over R=200mm bump extends nearly to the top wall, while it over R=40mm bump is limited to only a local area near the bump model surface. With an increase in S_{01}, the shock wave becomes weak and moves to a little upstream. For S_{01}=0.80 any obvious shock wave is not visible and there is only some weak wavelets. This results from the fact that the flow Mach number just upstream of the shock wave is reduced due to nonequilibrium condensation occurring over the bump model. In order to investigate the flow phenomenon at the foot of the shock wave over the bump, Fig.4 shows the surface flow patterns using the liquid crystal. With R=40mm bump model dry air flow separates just at the foot of the weak normal shock wave. This is due to the shock wave boundary layer interaction. With an increase in S_{01} the flow does not separates at the foot of the shock wave but separates at the just downstream of the shock wave. This boundary layer separation results from a sudden change of the flow area in the bump model and is different from the case of the dry air flow, which the flow separates due to an adverse pressure gradient caused by the shock wave. It is noted that the boundary layer separation at the foot of the shock wave is suppressed as S_{01} increases. However, with R=200mm model the flow does not separates at the foot of the shock wave or at any downstream location over the model. The surface flow patterns do not significantly change with S_{01}.

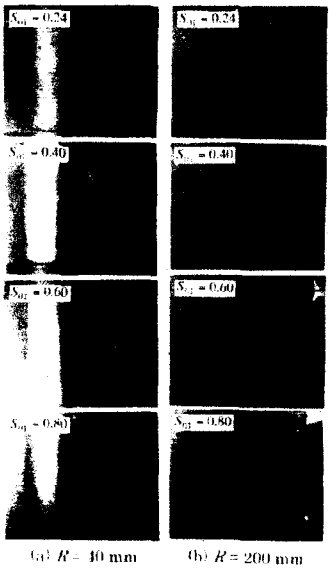

Fig. 4 Surface flow patterns

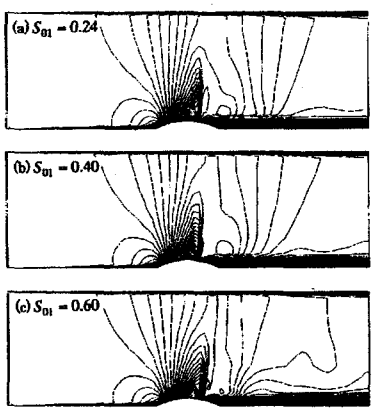

Fig. 5 Computed Mach number contours(R=40mm)

A comparison of the present computations and experiments can be found in Fig.5, in which Mach number contours are present for R=40mm bump model. As observed in Fig.3(a), the shock wave is nearly normal and limited to a local area over the bump model. It seems that the shock wave moves to upstream as S_{01} increases, causing weaker shock wave. This trend is quite similar to

the experimental results.

4.2 Pressure measurement

Fig.6 show static wall pressures over the bump model. For both the bump models the flow accelerates to a sonic speed at the bump apex and the flow becomes weak supersonic at the downstream of it.

This is terminated by the shock wave over the bump model. The static pressure decreases up to x/l=0.07 and then increases due to the shock wave. With an increase in S_{01}, the adverse pressure gradient of the shock wave seems to be reduced and the pressure recovery seems to be improved downstream. This results from the nonequilibrium condensation which occurs upstream of the shock wave. It is reasonable to conclude that nonequilibrium condensation suppresses the flow separation due to shock boundary layer interaction.

Fig.7 shows a comparison of the present computations and experimental results. Similar trends are found in both results, but the present computations seem to overpredict the static pressures over the bump model. The present computational results can be, however, accepted to be reasonable in that the bump model contains very complicated flow phenomena like shock boundary layer interaction and nonequilibrium as well.

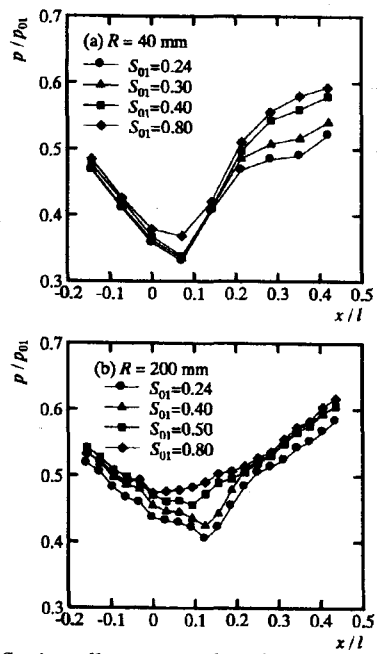

Fig. 6 Static wall pressures along bump model surface.

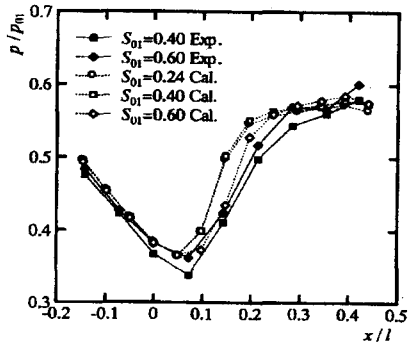

Fig. 7 Computed and measured static wall pressures

4.3 Effect of nonequilibrium condensation on pressure fluctuations

Fig.8 shows the experimental results of the fluctuating wall pressures over the bump models.

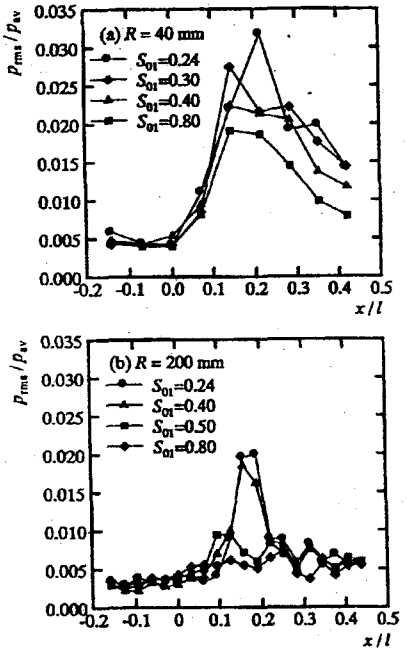

Fig. 8 Root-mean-square values of pressure fluctuations

Root mean square values P_{rms} of the fluctuating wall pressures are normalized by local mean pressure values. For R=40mm and S_{01}=0.24, the peak value of fluctuating wall pressure is about 3.3% of local mean pressure value and seems to occur at the foot of the shock wave. With an increase in S_{01}, the peak values seem to reduce and move to a little upstream. With regard to the effect of R on the fluctuating wall pressures, it seems that the peak values of fluctuating wall pressure decreases as R

increases. For the same S_{01} of 0.80, the peak value over the R=200mm bump model is much lower than that over R=40mm model. From the present experimental results, it is concluded that nonequilibrium condensation reduces the pressure fluctuations due to the shock boundary layer interaction. The interaction of the shock wave with the boundary layer becomes weak with an increase in S_{01}.
The fine droplets of the nonequilibrium condensation can influence the interaction as well. Detailed mechanism of the effects of the fine droplets on shock boundary layer interaction should be known to address this difficult problem. Further information of time scale of the fluctuating pressure signals can be obtained from a wavelet transform[15], as has frequently been applied to time-dependent data analysis. Using the fluctuating pressure signals, the present study has conducted the analysis of a continuous wavelet transform W(b,a) as described next.

For the time-dependent pressure signals p(t), the continuous wavelet transform W is defined by,

$$W(b,a)=\frac{1}{a^{1/2}}\int_{-\infty}^{\infty}\psi\left(\frac{t-b}{a}\right)p(t)dt \qquad (1)$$

Where ψ is a mother wavelet, a the scale parameter and b the location of time scale. Therefore the wavelet transform W(b,a) provides us multi-scale structures of the pressure signals on the (b,a) frame. The mother wavelet, called Morley wavelet[15], is given as,

$$W(t)=(b,a)=\exp(ik_{\psi}T)\exp\left(-\frac{T^2}{2}\right) \qquad (2)$$

$$T=\frac{t-b}{a} \qquad (3)$$

where k_{ψ} is a constant(k_{ψ} =6.0). The real part of the Morley wavelet above is symmetric with respect to T=0. The value of 1/a is taken to be the same as the frequency. Figs.9 and 10 show the experimental results obtained from the present wavelet transform analysis. The wavelet coefficient W(b,a) was plotted using the fluctuating pressure signals at measuring points S1 and S2, as shown in Fig.1. Each contour line means the line of W=0. From both the figures it is found that the dense region of the contours lines appears to be at equal intervals on the b-axis, being containing the range from high to low frequency. The dense region of high frequency results from boundary layer separation. For S_{01}=0.80 the contour lines in the region of high frequency become sparse rather, but in the low frequency region the contour lines are not significantly different from those of S_{01}=0.24.
This means that the nonequilibrium condensation suppresses the high frequency components of the fluctuating pressure signals, which are caused by the shock boundary layer interaction

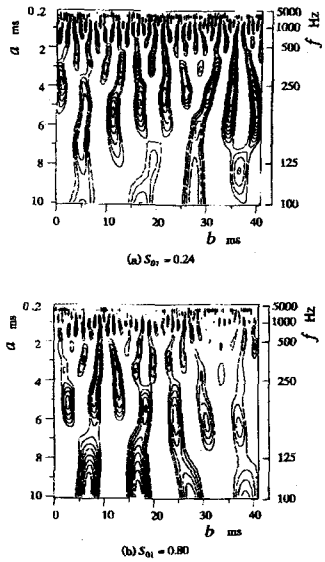

Fig. 9 Wavelet transform of time-dependent pressure signals(R=40 mm)

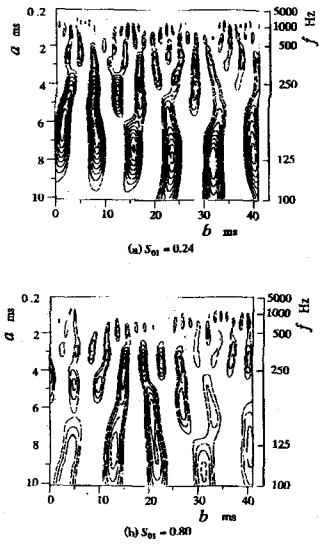

Fig. 10 Wavelet transform of time-dependent pressure signals(R=200 mm)

From the two results of Fig.9 and 10 it is also found that the bump geometry can influence the whole components of the fluctuating pressure signals.

4.4 Total pressure loss

Due to nonequilibrium condensation and shock wave, total pressure losses are expressed by entropy change next[16],

$$s - s_{01} = (1-\omega_{01})\frac{\Re}{Ma}\ln\left(T^{(\gamma_a/(\gamma_a-1))}\right) + (\omega_{01}-g)\frac{\Re}{M_v}\ln\left(T^{(\gamma_v/(\gamma_v-1))}/P_v\right) + g\left(-\frac{1}{\bar{r}}\frac{3}{\rho_l}\frac{\partial\sigma}{\partial T}\right) \quad (4)$$

$$\frac{s-s_{01}}{c_p} = \ln\left(\frac{T_0}{T_{01}}\right) - \frac{\Re}{M_m c_p}\ln\left(\frac{p_0}{p_{01}}\right) \quad (5)$$

Fig.11 show the contour lines of the total pressure (P_{01}-P_0)/P_{01}, where P_{01} means the total pressure upstream of the bump model and P_0 the local total pressure.

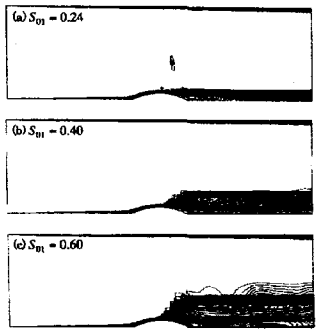

Fig. 11 Total pressure loss contours

The total pressure losses seem to be concentrating at the some regions, where shock wave, shear layer, and boundary layer occur. The region of the major total pressure loss expands with an increase of S_{01}. Consequently increase of S_{01} cause the strength of shock wave to reduce and boundary layer separation to suppress. In this study , it is not easy to discuss each of the major causes contributing to the total pressure losses. However from the point of view of the entire energy losses, the total pressure loss due to the nonequilibrium condensation should be considered.

5. Concluding Remarks

In order to investigate the effects of nonequilibrium condensation on the shock boundary layer interaction over a bump model, experiments were conducted using a supersonic indraft wind tunnel. Two-dimensional compressible Navier-Stokes equations were solved using the TVD MUSCL finite difference scheme. Computations represented the experimental results. Nonequilibirum condensation suppressed the separation and the pressure fluctuations caused by shock boundary layer interaction. Especially the nonequilibrium condensation was helpful to suppress the high frequency components of the pressure fluctuations. Further study is required to address detailed flow mechanism for the fine droplet effects on the shock boundary layer interaction.

References

[1] Wegener, P. P. ; Mach, L. M. : Condensation in Supersonic Hypersonic Wind Tunnels, Adv. In Appl Mech., Vol.5 pp.307-447 Academic Press., (1958).

[2] Matsuo, K. ; Kawagoe, S. ; Sonoda, K. ; Sakao, K. : Studies of Condensation Shock Waves(Part 1, Mechanism of their Formation), Bulletin of JSME, Vol.28, No.241, pp1416-1422, (1985).

[3] Zierep,J. and Lin,S., Bestimmung des Kondensationsbeginns Kondensation Bei Entspannung feuchter Luft in Ueberschallduesen, Forsch. Ing. –Wes., Vol.33, pp.169-172, (1967).

[4] Schnerr, G. H. ; Dohrmann, U. : Transonic Flow Around Airfoils with Relaxation and Energy Supply by Homogeneous Condensation, AIAA Journal., Vol.28, No.7, pp.1187-1193,(1990).

[5] Barschdorff, D. ; Fillipov, G. A. : Analysis of Certain Special Operating Modes of Laval Nozzles with Local Heat Supply, Heat Transfer-Society Research, Vol.2, No.5, p.76-87, (1970).

[6] Wegener, P. P. ; Cagliostro, D. J. : Periodic Nozzle Flow with Heat Addition, Combustion Science and Technology, Vol.6, pp.269-277, (1973).

[7] Saltanov, G. A. ; Tkalenko, R. A. : Investigation of Transonic Unsteady-State Flow in the Presence of Phase Transformations, J. of Appl. Mech. Tech. Phys., Vol.16, No.6, pp.857-878, (1975).

[8] Matsuo, K. ; Kawagoe, S. ; Sonoda, K. ; Setoguchi, T. : Oscillations of Laval Nozzle Flow with Condensation (Part 2, On the Mechanism of Oscillations and Their Amplitudes), Bulletin of JSME, Vol.28, No.235, pp.88-93, (1985).

[9] Sislian, J. P. : Condensation of Water Vapour with or without a Carrier Gas in s Shock Tube, UTIAS Rep.201, (1975).

[10] Kim,H.D.; Setoguchi,T. : Passive Condensation Shock Wave in a Transonic Flows, Intl. Jour. Heat and Mass Transfer, 2000(submitted)

[11] Setoguchi,T.; Kim.H.D. : Passive Control of Condensation Shock Oscillations in a Transonic Nozzle, Intl. Jour. Heat and Mass Transfer, 2000(submitted)

[12] Wegener, P. P. : Wu, B., Nucleation Phenomena, pp.325,(1977).

[13] Mills, A. F. ; Seban, R. A. : The Condensation Coefficient of Water, Int. J. Heat Mass Transf., Vol.10, pp.1815-1827,(1967)

[14] Kirkwood, J. G. ; Buff, F. P. : The Statistical Mechanical Theory of Surface Tension, J. Chem. Phys., Vol.17, pp.3389-3343, (1949).

[15] Farge,M. : Wavelet Transforms, Their Applications to Turbulence, Annual Review of Fluid Mechanics, Vol.24, pp.395-457, (1992)

[16] Sugawara,M.; Oshima,N. : Analysis of Condensation in Supersonic Nozzles, Proc. 12th Intl. Symp. on Combustion, pp.1193-1201, (1968)